Whole-Body *in Vivo* MPI Cytometry Reveals Injection Route-, Dose-, Cell Size- and Disease-Dependent Differences in Organ Biodistribution

Ali Shakeri-Zadeh[1,2], Shreyas Kuddannaya[1,2], Chengyan Chu[3], Kritika Sood[1,2], Asif Itoo[1,2], Cristina Zivko[4,5], Aline M. Thomas[1,2], Vasiliki Mahairaki[4,5], Piotr Walczak[3], Jeff W.M. Bulte[1,2,6,7,8,9*]

[1]The Russell H. Morgan Department of Radiology and Radiological Science, Division of MR Research, The Johns Hopkins University School of Medicine; Baltimore, MD, USA. [2]Cellular Imaging Section and Vascular Biology Program, Institute for Cell Engineering, The Johns Hopkins University School of Medicine; Baltimore, MD, USA. [3]Center for Advanced Imaging Research, Department of Diagnostic Radiology and Nuclear Medicine, University of Maryland; Baltimore, Maryland, USA. [4]Department of Genetic Medicine, Johns Hopkins University School of Medicine, Baltimore, MD, USA. [5]The Richman Family Precision Medicine Center of Excellence in Alzheimer's Disease, Johns Hopkins University School of Medicine, Baltimore, MD, USA. [6]Department of Biomedical Engineering, The Johns Hopkins University School of Medicine; Baltimore, MD, USA. [7]Department of Oncology, The Johns Hopkins University School of Medicine; Baltimore, MD, USA. [8]Department of Chemical & Biomolecular Engineering, The Johns Hopkins University Whiting School of Engineering; Baltimore, MD, USA. [9]F.M. Kirby Research Center for Functional Brain Imaging, Kennedy Krieger Institute; Baltimore, MD, USA.

*Corresponding author. jwmbulte@mri.jhu.edu

Short title: Whole-body in vivo MPI cytometry of cellular therapeutics

One sentence summary (teaser): Whole-body *in vivo* cytometry using MPI is able to dynamically track and quantify tissue stem cell distribution.

Abstract

Robust quantification of the whole-body biodistribution of cellular therapeutics remains a major challenge. We performed *in vivo* cytometry using magnetic particle imaging (MPI) to track magnetically labeled cells on a time scale of minutes with high sensitivity, zero background signal, and simple linear quantification. Human mesenchymal stem cells (hMSCs, ~25 μm) and human neural precursor cells (hNPCs, ~10 μm) were labeled with superparamagnetic iron oxide nanoparticles, and mapped with MPI after intravenous (IV) or intra-arterial (IA) injection in normal mice. The tissue site and numbers of cell accumulation and retention were dependent on cell size, cell dose, injection frequency and injection route, with the lung and liver serving as the major entrapment organs. In mice with experimental autoimmune encephalomyelitis, but not in normal mice, hMSCs also homed to the spleen. Integrating MPI cytometry with cell therapy may aid in further optimization of the route, dose, and frequency of cell administration.

INTRODUCTION

Developing non-invasive *in vivo* cytometry methods to longitudinally track and quantify therapeutic stem cells and immune cells remains an active area of research to successfully translate cell therapies into clinical practice (*1*). It has been shown that cell injections can miss their target in up to 50% of patients even when injected under ultrasound imaging-guided injections (*2*), emphasizing the need for more effective methods to monitor and improve cell delivery (*3*). Traditional imaging modalities for *in vivo* cytometry or quantitative cell tracking often fall short in providing the necessary sensitivity, specificity and quantification required for precise whole-body cell tracking. ^{1}H magnetic resonance imaging (MRI) cell tracking (*2, 4, 5*) lacks the specificity and accuracy needed to quantify magnetically labeled cells with reliable whole-body biodistribution after systemic delivery. Nuclear imaging, either positron emission tomography (PET) or single photon emission computed tomography (SPECT), is a quantitative method and offers high sensitivity for cell tracking but involves ionizing radiation and lacks spatial resolution (*6*). Optical imaging suffers from limited tissue penetration and quantification difficulties (*7*). Magnetic particle imaging (MPI) has emerged as a promising modality for *in vivo* cell tracking (*8-11*) with a reported *in vivo* detection sensitivity as low as 250 labeled cells (*12*). MPI directly detects superparamagnetic iron oxide (SPIO) nanoparticles with high sensitivity and specificity (*13, 14*). Importantly, MPI provides a linear relationship between signal intensity and SPIO concentration, enabling accurate quantification of SPIO-labeled cells and tracers (*8, 10, 15*). ^{19}F MRI has been explored as an alternative quantitative cell tracking approach for *in vivo* cytometry (*16*), but it suffers from lower sensitivity and temporal resolution compared to MPI (*17*). The main limitations of MPI include its relatively low spatial resolution and its lack of anatomical context, necessitating its combination with imaging modalities such as MRI or computed tomography (CT) for accurate anatomical localization. Recent progress in the development of human-scale MPI scanners demonstrates that the technology is scalable and positioned for clinical translation (*18-21*).The use of nonionizing magnetic fields in MPI (*22*), combined with the biocompatibility and minimal functional impact of the magnetic labeling of cells (*23*), supports the future use of clinical MPI for real-time cell tracking.

Here, we introduce the concept of *in vivo* MPI cytometry, an imaging approach that enables dynamic whole-body tracking and quantification of SPIO-labeled therapeutic cells in living subjects on a time scale of minutes. A schematic overview of the MPI cytometry workflow

is shown in **Fig. 1** to illustrate the experimental sequence and integration of the various methodological components.

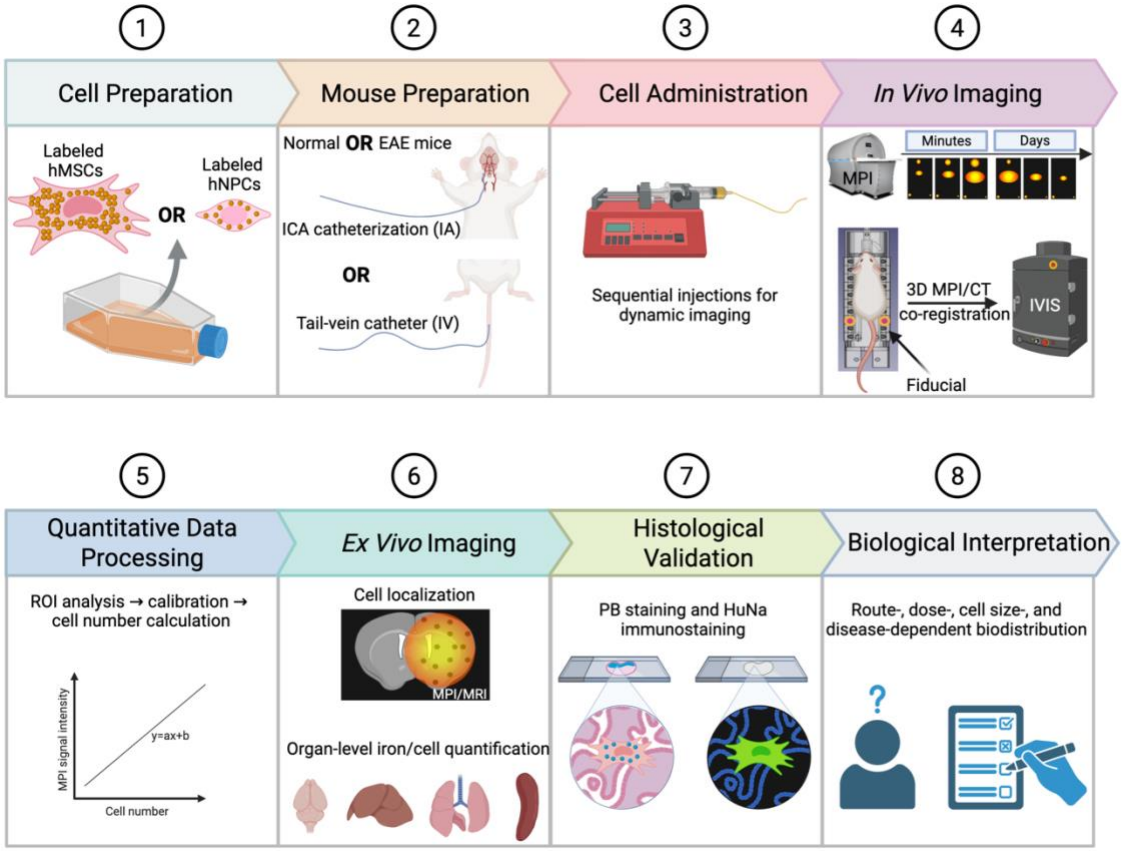

Figure 1: **Schematic overview of the MPI cytometry setup and experimental workflow** (Created in BioRender. Shakeri-Zadeh, A. (2025) https://BioRender.com/jy252vx).

Implementing the labeled cell-fiducial calibration strategy, in which reference tubes containing known numbers of labeled cells from the same batch used for injection are imaged alongside each animal, is central to our MPI cytometry workflow and enables direct conversion of organ MPI signal into cell numbers both *in vivo* and *ex vivo*. Most if not all studies as of today have used fiducials containing simple aqueous solutions of suspended SPIO particles, but it has now become clear that these fiducials do not mimic labeled cells (*24*) and tissue (*25*). *In vivo* MPI cytometry was performed on two distinct stem cell types, i.e., human mesenchymal stem cells (hMSCs), which are relatively large cells (~25 µm in diameter or 8,000 μm^3 for a spherical volume, which the cells have following trypsinization before injection) used before in pre-clinical MPI (*8, 26*) and clinical MRI (*27*) cell tracking studies, and human neural precursor cells (hNPCs), representing smaller cells (~10 µm in diameter or ~500 μm^3 volume) used with MRI

cell tracking (*28*). Selecting these two distinct human stem cell types allows a direct comparison of the impact of cell size and delivery route on whole-body biodistribution. Our results reveal distinct biodistribution profiles for the two cell types, highlighting the suitability of MPI cytometry for quantitative monitoring of cell distribution *in vivo*. Although MPI has been previously used to track cells *in vivo* (*10, 26, 29*), cells were injected intraparenchymally in tissue (no systemic injection) or imaged at much later time points, without initial fast dynamic quantitative imaging at a time scale of minutes. To broaden the biological relevance of *in vivo* MPI cytometry and highlight its utility beyond assessment of the baseline biodistribution, we also applied the method in an experimental autoimmune encephalomyelitis (EAE) neuroinflammatory disease model and were able to identify the spleen as a key site of hMSC accumulation following systemic administration. The detection of SPIO-labeled hMSCs in the spleen, validated by both MPI and histological analysis, supports the concept of systemic immunosuppression (*30-32*), wherein hMSCs exert anti-neuroinflammatory effects through remote splenic cell-cell interactions. This observation underscores the potential of MPI to further uncover mechanistic insights into the biodistribution and therapeutic action of systemically delivered stem cells.

RESULTS

Whole-body quantitative *in vivo* MPI cell tracking

hMSCs were efficiently labeled with SPIO (**Fig. 2A**). *In vivo* MPI/CT imaging revealed distinctly different biodistribution profiles for IV compared to IA injection (**Fig. 2B,C**). At 30 min post-IV injection cells accumulated within the lungs, with negligible signal in liver and brain, indicating pulmonary entrapment. In contrast, IA injection revealed cell localization in the brain, lungs, and liver. After 1 day, IV-injected cells completely redistributed to the liver, while IA-injected cells persisted in both brain and liver without lung signal (**Fig. 2B**). Using a calibration curve for the same batch of labeled hMSCs that were injected, the number of cells at 30 min post-IA injection were calculated to be 99,937±10,392 for the lung/liver and 27,500±2,240 cells for the brain. These total numbers summing up to approximately 125,000 cells closely equals the amount of 120,000 injected cells, translating to an iron mass of 57 pg Fe per cell as estimated from signal intensity and known Fe content determined using a Ferrozine assay.

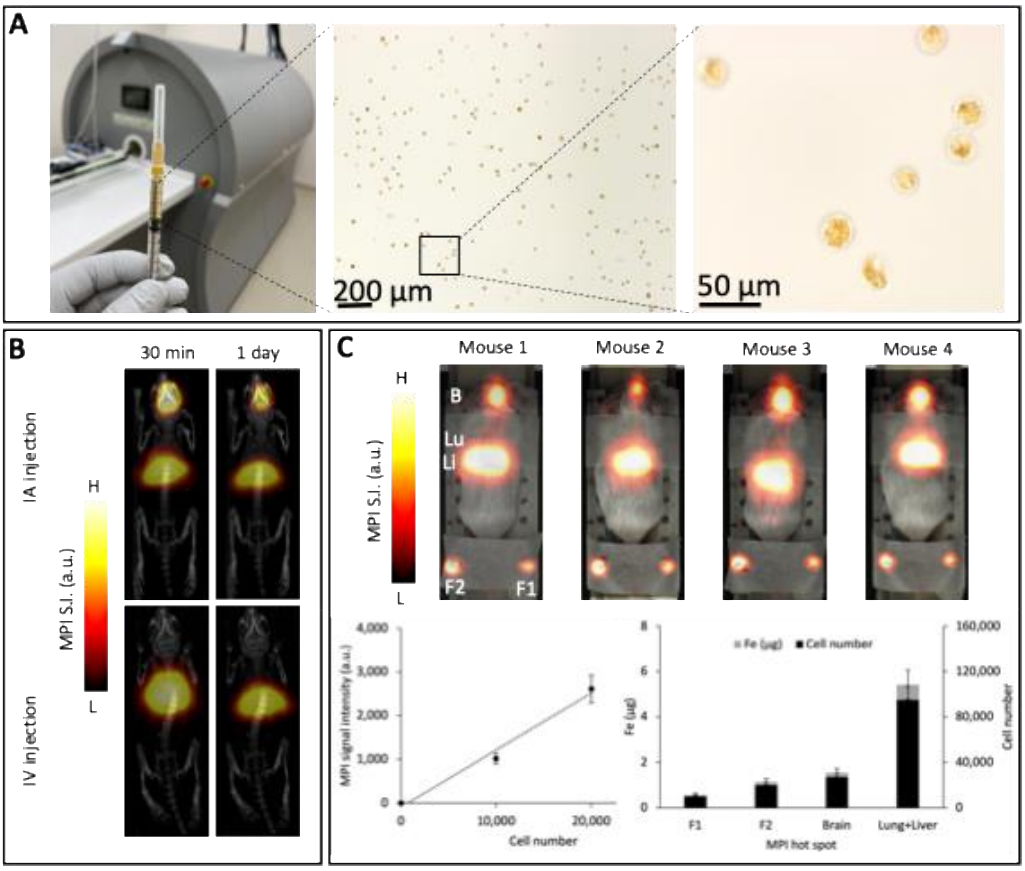

Figure 2: Whole-body *in vivo* tracking and quantification of hMSCs following IV or IA injection. (**A**) Macro- and microscopic visualization of ferucarbotran-labeled hMSCs before injection. (**B**) *In vivo* MPI/CT images of labeled hMSCs at 30 min and 1 day after IV or IA injection. (**C**) Quantitative analysis of cell accumulation 30 min post-IA injection. Two fiducials (F1=10,000 and F2=20,000 labeled cells) were used for calibration (y=0.13x-94.92; R^2=0.98). Data in each figure panel represent three independent experiments. B, Lu, Li, and F stand for brain, lungs, liver and fiducials, respectively.

Bimodal MPI/MRI cell tracking

To validate the cerebral delivery of ferucarbotran-labeled hMSCs following IA injection, we performed *ex vivo* magnetic imaging (**Fig. 3A**) and histological analysis (**Fig. 3B**). Coronal MRI scans showed unilateral hypointense regions across multiple brain slices, consistent with labeled cell accumulation. The signal voids were present from midbrain to forebrain, indicating a global cell distribution in the entire ipsilateral hemisphere. MPI scans of the same brains revealed hot spots that overlapped with the MRI hypointensities. Histological Prussian blue staining further confirmed the presence of SPIO-labeled hMSCs. Anti-human nuclear antigen

(HuNa) staining revealed that the iron-loaded cells contained human nuclei, confirming they were indeed the hMSCs that were injected, corroborating the MRI/MPI findings.

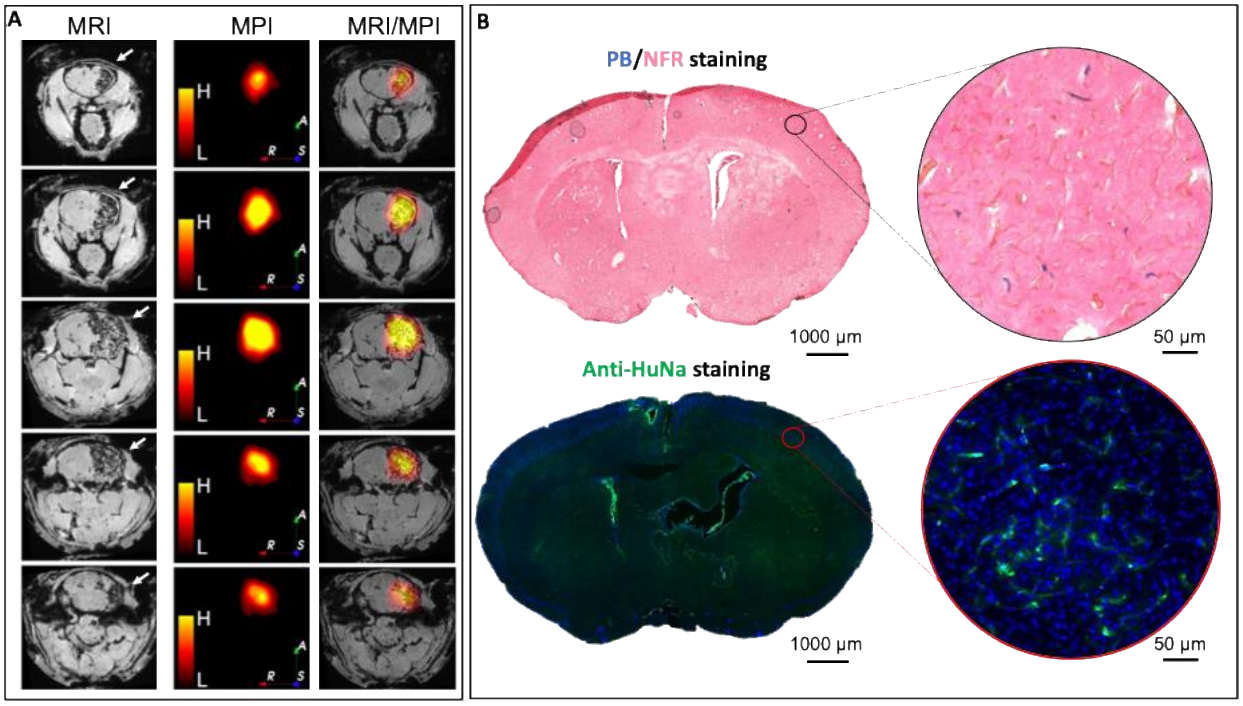

Figure 3: Bimodal MPI/MRI of hMSCs at 6 hours after IA injection. (**A**) Consecutive coronal *ex vivo* MRI, MPI, and MRI/MPI overlay images showing MRI hypointensities (white arrows) and MPI hot spots from midbrain to forebrain, corresponding to labeled hMSCs. (**B**) Corresponding coronal brain sections stained for iron (top row) and anti-HuNa (bottom row), demonstrating that the remains localized in hMSCs.

Longitudinal MPI cell tracking

To investigate the long-term biodistribution and persistence of IA-injected cells, we performed serial *in vivo* and *ex vivo* MPI scans at 6 h (day 0), 2 days, 7 days, and 30 days post-injection of 120,000 SPIO-labeled hMSCs (**Fig. 4A**). Using two fiducials containing labeled hMSCs from the same batch that was injected, MPI signal quantification revealed 22,294±1,920 cells in the brain and 114,940±13,125 cells in the lungs/liver on day 0 (**Fig. 4B**). By day 2, the brain signal became undetectable *in vivo*, indicating that most cells redistributed from the brain to other organs. The lungs and liver retained 117,385±14,450 cells at Day 2, reflecting the early loss of brain-localized cells and sustained hepatic/pulmonary retention. The cell number in liver declined to 58,835±5,210 at day 7 and 24,280±2,225 at day 30. *Ex vivo* MPI confirmed these observations with no detectable cells in the heart. At Day 0, 8,200±970 cells were detected in the brain, 5,430±436 in the lungs, and 102,500±11,240 in the liver, providing a (lung+liver)/brain

ratio of ~13. By day 2, only 2,330±190 cells remained in the brain and no cells were detected in the lungs, while the liver signal increased to 108,800±8,425 cells, yielding a (lung+liver)/brain ratio of ~47. At days 7 and, the liver retained 67,300±7,360 and 22,240±2,015 cells, respectively, with no detectable cells in the lungs or brain. These findings suggest a possible redistribution of SPIO-labeled cells from the lungs and brain into the liver between days 0 and 2, followed by gradual clearance.

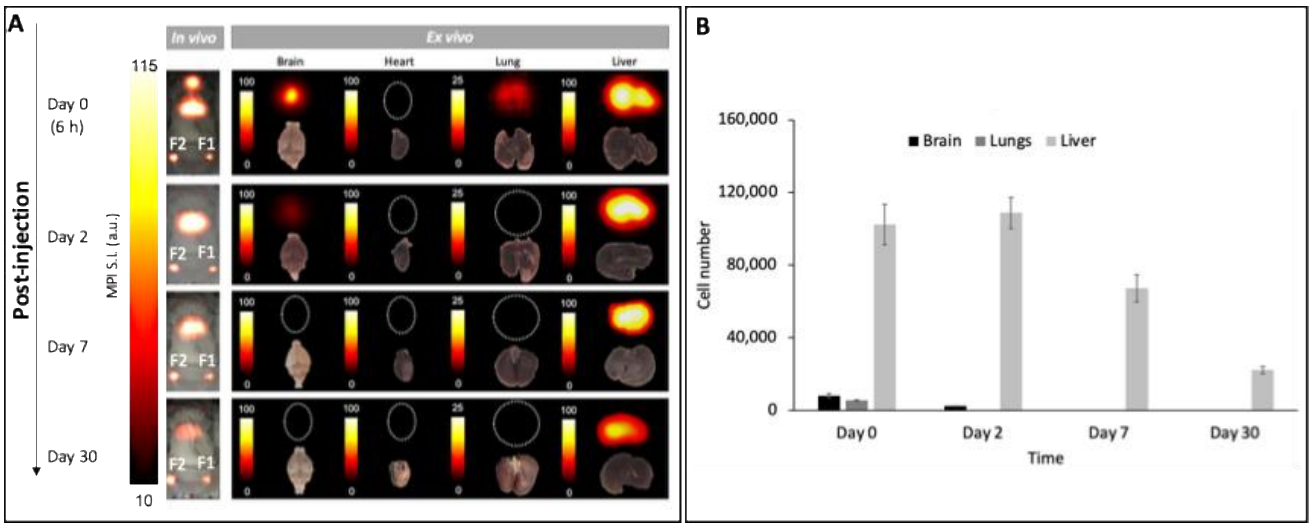

Figure 4: Longitudinal MPI of labeled hMSCs after IA injection. (**A**) *In vivo* and *ex vivo* MPI at different time points post-injection. Color-coded heat maps indicate signal intensity. Dotted circles highlight organs with no detectable signal. Shown are representative data from three independent experiments. (**B**) *Ex vivo* MPI-based quantification of labeled hMSCs. Similar to the *in vivo* studies, F1=10,000 and F2=20,000 labeled cells were used as fiducials for *ex vivo* quantification.

Fast dynamic whole-body *in vivo* MPI cytometry: effect of cell size

To compare the *in vivo* biodistribution of two stem cell types having different sizes, we performed dynamic MPI tracking of 120,000 IA-injected ferucarbotran-labeled hMSCs and 960,000 Synomag®-D70-labeled human neural precursor cells (hNPCs), have spherical diameters of ~25 and 10 µm following trypsinization, respectively (**Fig. 5**). Each total cell dose was injected using four incremental injections, with equal cell numbers delivered in each injection. Both cell types were effectively labeled as confirmed with PB staining. For hMSCs serial *in vivo* MPI performed over 12 minutes post-injection revealed a prominent signal in both the brain and the liver/lung regions, with the signal increasing over time from 0 to 12 min. Using a calibration curve obtained from fiducials containing known numbers of labeled cells from the

same batch as was injected, it could be calculated that 22,569±1,805 hMSCs localized in the brain, with 112,808±10,600 cells in the combined liver and lung regions, yielding a (lung+liver)/brain ratio of ~5. The labeled hMSCs were also quantified using *ex vivo* MPI (**Fig. 6A**), which detected 10,614±1,004 cells in the brain, 7,212±820 in the lungs, and 92,140±10,437 in the liver. The total calculated distribution numbers of 135,000 (*in vivo* MPI) and 110,000 (*ex vivo* MPI) are in close agreement with the total amount of injected cells, being 120,000 (**Table 1**).

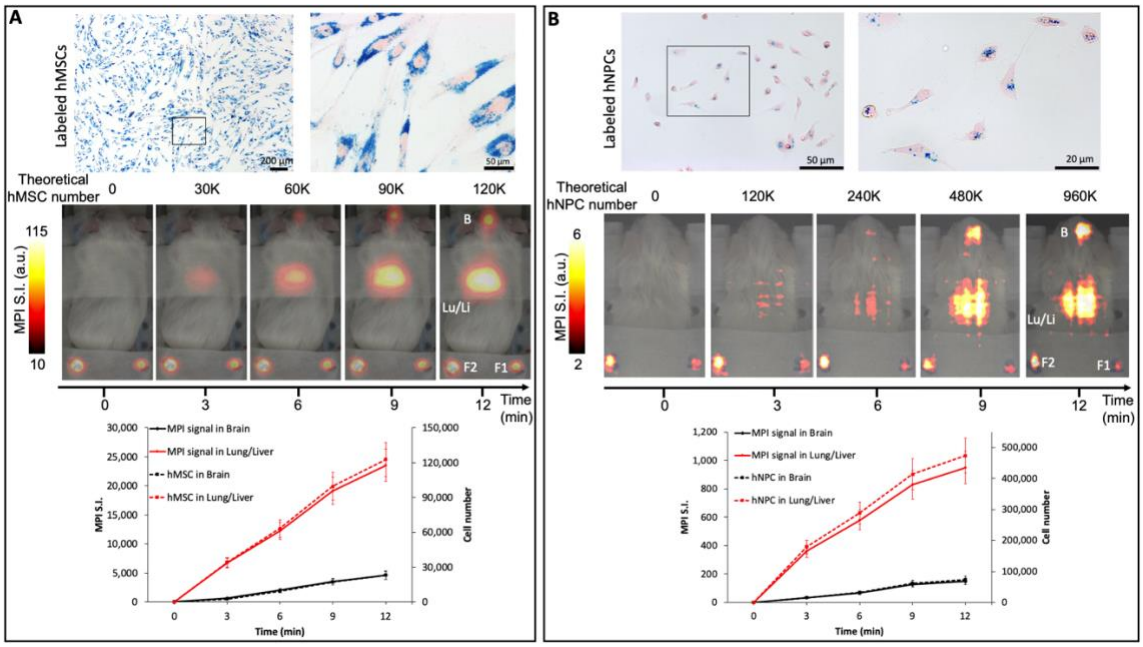

<u>Figure 5:</u> Dynamic *in vivo* MPI cytometry comparison of labeled hMSCs (A) and hNPCs (B) after IA injection. Top panels show PB staining to confirm intracellular iron accumulation in each cell type. **Middle panels** display time-lapse MPI scans at multiple time points post-injection. B=brain, Lu/Li=lung/liver. Fiducials F1 and F2 contain 10,000 and 20,000 labeled hMSCs in panel (A), and 20,000 and 40,000 labeled hNPCs in panel (B), respectively, from the same batch as injected cells. The calibration equations used were: y=0.1868x+220 (R^2=0.99) for hMSCs and y=0.0021x–2 (R^2=0.99) for hNPCs. **Bottom panels** present quantitative plots of MPI signal intensity (arbitrary units) and calculated cell numbers over time in each region, demonstrating the ability of MPI for both fast localization and dynamic quantification of labeled cells. Data represent three independent experiments.

For the smaller hNPCs (**Fig. 5B**), the *in vivo* MPI demonstrated a dynamic signal evolvement in the same anatomical regions. At 12 min post injection, ~57% of injected hNPCs were detected *in vivo*, including 74,240±6,854 hNPCs in the brain and 474,580±39,094 cells in the lung and liver, corresponding to a (lung+liver)/brain ratio of approximately ~6.5, i.e. ~30% higher than the corresponding ratio observed for hMSCs. The ~43% discrepancy between the

injected and detected hNPCs may be attributed to several factors, including diffuse biodistribution below the MPI detection threshold and the inherently lower iron loading of hNPCs relative to hMSCs. Additionally, limited spatial resolution and spillover effect in MPI, particularly from high-signal regions such as the liver, may obscure weak or widely dispersed signals, further contributing to underestimation. *Ex vivo* MPI (**Fig. 6B**) detected only 3,420±280 cells in the brain, no cells in the lungs, and 143,540±12,430 cells in the liver (**Table 1**). Histological analysis with PB staining and anti-HuNa immunolabeling only confirmed the presence of SPIO-labeled human cells in the hMSC-injected brains. As hNPCs are much smaller than hMSCs this could have resulted from a larger wash-out during post-mortem processing compared to hMSCs. Although MPI revealed substantial accumulation of labeled hMSCs in the liver and lungs as well as accumulation of labeled hNPCs in the liver, histological analyses failed to corroborate the corresponding MPI signals. This apparent discrepancy may be attributed to multiple technical and biological factors. First, MPI offers high sensitivity and full-organ detection capability, while histology is inherently limited to thin tissue sections and may miss sparsely distributed cell populations. Second, cells trapped in the microvasculature, especially within the brain, may be lost during organ removal and perfusion, leading to false negatives in post-mortem histological analysis. Similarly, in the liver and lungs, cells may localize transiently within sinusoidal spaces or vascular compartments and be washed out during fixation and sectioning.

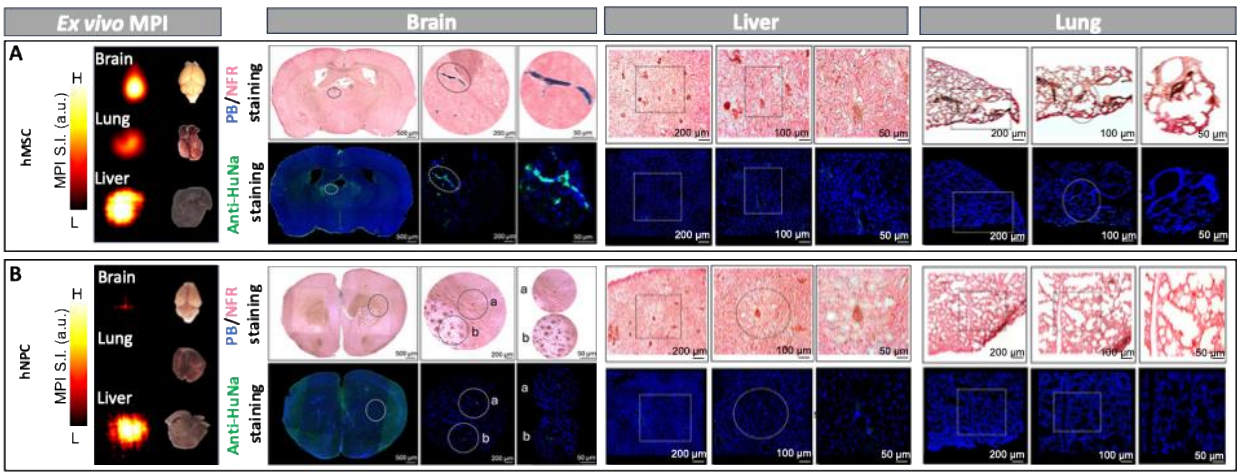

Figure 6: ***Ex vivo* MPI and histology validate cell localization in major organs.** Representative *ex vivo* MPI and histological analysis of ferucarbotran-labeled hMSCs (**A**) and SynomagD-70-labeled hNPCs (**B**) 6 hours after IA-injection. Co-localization of positive PB and anti-HuNA staining confirms the presence of SPIO-labeled hMSCs in the brain.

Table 1: *In vivo* and *ex vivo* MPI cytometry of SPIO-labeled hMSCs and hNPCs.

Parameter	hMSCs	hNPCs
Injected cell dose	120,000	960,000
Cell size (µm)	~25	~10
***In vivo* MPI (12 min post injection)**		
Brain (mean ± SD)	22,569±1,805	74,240±6,854
Lung + Liver (mean ± SD)	112,808±10,600	474,580±39,094
Total detected cells	135,377	548,820
% of injected cells detected	113%	57.2%
***Ex vivo* MPI (6 hours post injection)**		
Brain (mean ± SD)	10,614±1,004	3,420±280
Lungs (mean ± SD)	7,212±820	Not detected
Liver (mean ± SD)	92,140±10,437	143,540±12,430
Lung + Liver (mean ± SD)	99,352±10,719	143,540±12,430
Total detected cells	109,966	146,960
% of injected cells detected	91.6%	15.3%

Splenic localization of hMSCs in the EAE disease model

After establishing the robustness of our MPI cytometry approach in normal mice, we applied the method to an inflammatory setting to evaluate its utility for quantitative *in vivo* cell tracking under disease conditions. To this end, we performed biodistribution studies in EAE mice as a model of multiple sclerosis (MS), and dynamically tracked 500,000 IV-delivered ferucarbotran-labeled hMSCs (**Fig. 7**). We selected hMSCs for these experiments because they are among the most widely used therapeutic cell types in preclinical (*33*) and clinical (*34*) MS studies and are known to exert potent immunomodulatory effects (*35*). Fast dynamic MPI following four sequential IV injections (**Fig. 7A**) revealed that labeled hMSCs were initially retained predominantly in the pulmonary and hepatic compartments. Within hours, however, a distinct MPI signal emerged in the spleen (**Fig. 7B**), indicating redistribution of a fraction of the injected cells to secondary lymphoid tissue. By one day, MPI hotspots were detected in the lungs, liver, and spleen, whereas by one week post-injection, only hepatic and splenic signals remained. To the best of our knowledge, this represents the first *in vivo* MPI visualization of

splenic localization of hMSCs in EAE mice following IV delivery. *Ex vivo* MPI corroborated these findings, quantifying 61,450±8,230 hMSCs in the spleen (**Fig. 7C**). Histological analysis further validated both *in vivo* and *ex vivo* MPI findings. PB staining (**Fig. 7C**) showed discrete iron-positive foci distributed primarily within the white pulp (leukocyte) region, although to some extent also in the red pulp. Anti-human nuclear antigen (HuNa) immunofluorescence staining (**Fig. 7C**) confirmed co-localization of HuNa–positive cells in these areas, confirming that most of the SPIO particles originated from hMSCs instead from endogenous iron present in the red pulp and/or murine macrophages that had phagocytosed SPIO from MSCs.

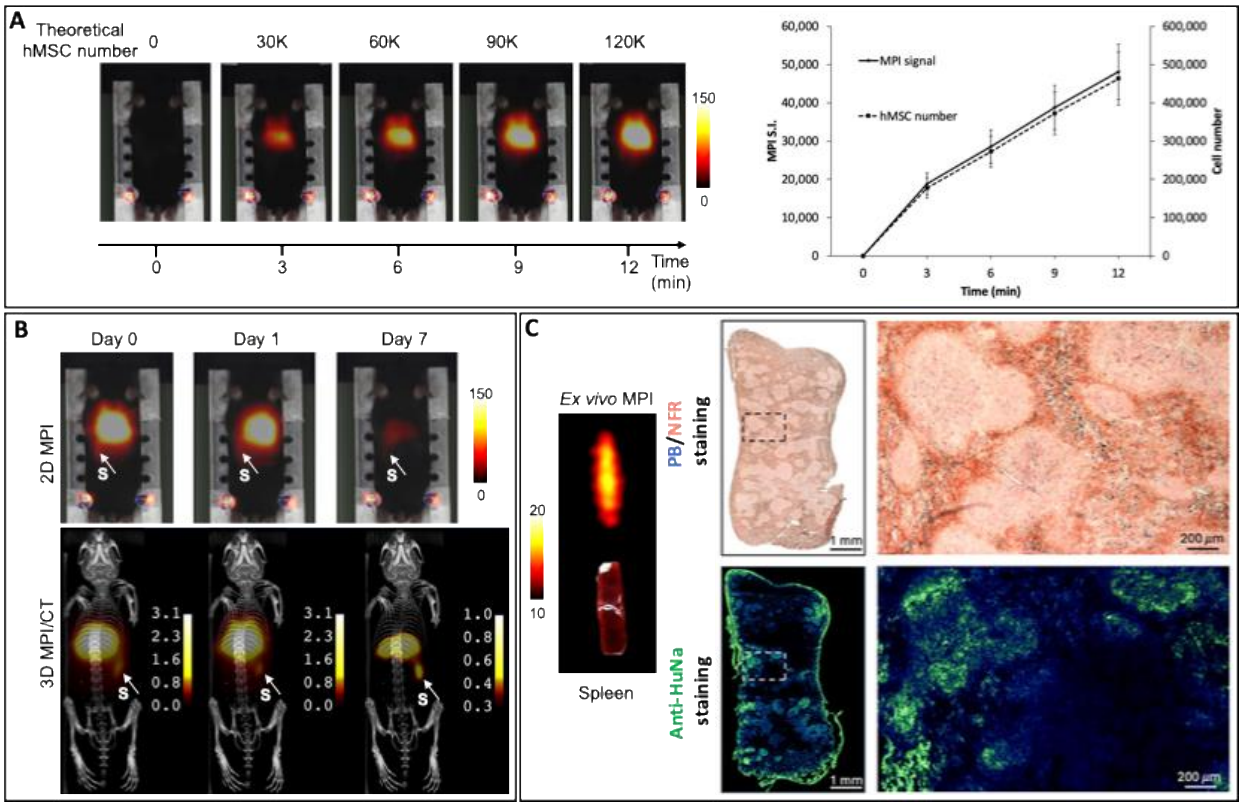

<u>Figure 7:</u> *In vivo* and *ex vivo* MPI cytometry of IV-injected ferucarbotran-labeled hMSCs in EAE mice. (A) Representative real-time *in vivo* MPI data obtained following four sequential IV injections, totaling 500,000 labeled hMSCs. Serial 2D MPI acquisitions (0–12 min) reveal rapid signal build-up in the lung/liver region, enabling minute-scale cytometry. Quantification was performed using the fiducial-based regression method (y=0.10x+641.8, R^2 = 0.98), described above for the normal mice. Error bars in the graph represent the standard deviation of MPI signal intensity. **(B)** Longitudinal tracking of the same mouse using 2D MPI (top) and 3D MPI/CT (bottom) at 2 h (day 0), 1 day, and 1 week post-injection. A distinct MPI hot spot appears in the spleen (white arrows, S=spleen) beginning at 2 h and persists through later time points, indicating hMSC redistribution from the pulmonary/hepatic compartments to secondary lymphoid tissue. **(C)** *Ex vivo* MPI of the spleen harvested from the same animal,

confirming *in vivo* splenic signal. PB staining (top right) shows iron-positive foci co-localizing with HuNa–positive cells (bottom right), validating the presence of SPIO-loaded hMSCs within the splenic immunoactive zone of the white pulp. Color bars in each panel show MPI signal intensity (a.u.).

DISCUSSION

Route of delivery: IA vs. IV cell injection.

The findings in this study show how the route of cell delivery largely influences the initial biodistribution and subsequent homing. IA injection of SPIO-labeled cells led to a considerably different organ distribution compared to IV injection. Consistent with numerous prior imaging studies, IV-injected hMSCs underwent a first-pass sequestration in the lung vasculature (*26, 36*). This well-known "pulmonary trap" is attributed to the large size (18–30 μm diameter) and adhesive properties of hMSCs, which cause 50–80% of IV injected cells to lodge in the pulmonary capillaries (*36*). Our MPI data are in alignment as we observed a strong MPI signal concentrated in the lungs 30 min after IV injection (**Fig. 2B**). This mirrors previous reports using both optical and nuclear imaging. Bioluminescence imaging of luciferase-expressing hMSCs shows a bright lung signal within minutes of IV injection, which diminishes over 1–2 days as cells clear or die (*36*). Similarly, SPECT and PET tracking of radiolabeled hMSCs have documented that IV injected cells accumulate first in lungs (*36, 37*), with a subsequent redistribution in the liver (*38*). Consequently, only a small fraction of hMSCs can reach certain targeted tissues after IV injection. Delivering cells via a targeted arterial route allows a greater proportion of injected cells to reach the intended organ. In our study, IA injection greatly enhanced cell delivery to the brain, whereas an IV injection with an ~8-fold higher dose yielded no detectable brain MPI signal. This observation aligns with prior reports using other modalities. T2-weighted MRI demonstrated that IA transplantation of hMSCs led to markedly enhanced cell homing in the brain of stroked rats, while IV injection of the same cells produced negligible brain localization (*39*). However, IA injection of hMSCs may carry a risk of microvascular blockage (*39*) and hence its safety must be carefully considered in terms of cell size and cell dose (*40*). Nevertheless, the ability of IA administration to bypass the lung "barrier" and achieve near whole-body distribution is a clear advantage for targeting organs beyond the pulmonary circuit, as demonstrated for targeted renal delivery of hMSCs to the kidney using the renal artery (*41*), or bone marrow stem cells to the pancreas and spleen using the superior pancreaticoduodenal artery or splenic artery, respectively (*42*).

By combining dynamic tracking, cell quantification, and disease-model validation, MPI cytometry can elucidate mechanistic principles such as cell size–dependent entrapment, delivery route–specific organ targeting, and disease-driven redistribution, that are difficult or impossible to obtain with conventional imaging modalities. These insights highlight the conceptual breadth of *in vivo* MPI cytometry and its relevance for guiding therapeutic cell delivery strategies.

Cell size differences: hMSCs vs. hNPCs

Beyond the delivery route, the intrinsic properties of the cells led to marked differences in biodistribution and organ retainment (**Fig. 5**). A robust brain signal could only be observed after injection of 480,000 hNPCs. A major determinant of the cell type–dependent biodistribution is cell size. hMSCs average ~25 μm in diameter (with reported ranges up to 31 μm) (*43*), whereas hNPCs measure ~9–12 μm. Because both cell types exceed the 5–8 μm diameter of brain capillaries, their initial localization after IA delivery is governed primarily by passive, size-dependent microvascular trapping. This mechanical first-pass entrapment explains the stronger cerebral retention of hMSCs compared to the smaller hNPCs.

MPI vs. other conventional tracking modalities

MPI enables a level of cell tracking sensitivity and quantification that addresses many limitations of established imaging modalities (MRI, PET/SPECT, and optical imaging). A major advantage of MPI is the ability to quantitatively track small cell populations in deep tissue with high specificity (**Fig. 3**), as there is no background signal. Hence, there is no ambiguity in identifying SPIO-labeled cells (*14, 26*). This specificity contrasts with conventional MRI of SPIO-labeled cells, which relies on negative contrast that can be confounded by endogenous sources (e.g. air/tissue interfaces, hemorrhage, or calcifications). Hence, linear quantitation of iron using MPI enabled us to convert image signal directly into cell number estimates, which is not feasible with MRI. As a result, we could "non-invasively" count the number of cells, i.e., perform "*in vivo* cytometry" in each organ over time. We are able to detect and quantify cell numbers in the order of thousands with MPI *in vivo*, which is in line with published sensitivity benchmarks. A recent direct comparison showed that MPI can detect as few as 4,000 hMSCs (approximately 75 ng of iron) in a mouse, whereas ^{19}F MRI may be required on the order of 250,000 cells for detection (*17*). Another remarkable advantage of MPI is its capacity for its

dynamic imaging. We leveraged fast scanning and the lack of tissue attenuation in MPI to monitor cell biodistribution immediately after injection and then repeatedly over days to weeks. Such data are difficult to obtain with other modalities. Optical imaging cannot be used in deep organs with tissue attenuation, while ^{19}F MRI requires lengthy scans. Acquiring just eight contiguous 5.0 × 2.8 cm (2-mm thick) slices with ^{19}F MRI takes approximately 2 hours, without whole-body coverage (*16*). MPI enables rapid whole-body imaging of mice, requiring only 1–2 min for 2D scans, depending on imaging parameters such as scan mode. Recent work has demonstrated real-time "fluoroscopy" with MPI, tracking labeled cells moving through a flow system at sub-second time frame rates (*44*). Our studies did not require sub-second time frames, but we did acquire serial whole-body snap shots immediately post-injection to observe the first-pass distribution. The ability to see cells in near real-time opens the door to optimizing injection techniques (e.g., slow vs. bolus injection, use of magnetic targeting, etc.) in ways that static endpoint measurements cannot.

Although MPI currently achieves a practical spatial resolution of approximately 1 mm (*45*), which can be enhanced to ≤300 µm with optimized SPIO tracers and pulse sequences (*46*), its current resolution remains comparable to that of preclinical PET (~1–2 mm) (*47*) and ^{19}F MRI (~0.8 mm) (*16*). However, it still lags behind the sub-100 µm resolution achievable with high-field conventional MRI. The limited spatial resolution of MPI can be effectively mitigated by co-registering MPI with high-resolution MRI (**Fig. 3A**), allowing the superimposition of quantitative MPI-based cell tracking onto detailed anatomical maps for accurate and spatially resolved cytometry.

Taken together, our experiments establish MPI as a robust *in vivo* cytometry platform capable of dynamic, organ-specific quantification of SPIO-labeled cells in deep tissues on a time scale of minutes and across multiple days, capabilities not demonstrated in prior MPI cell tracking studies. MPI provides a highly sensitive, background-free detection of labeled cells but lacks intrinsic anatomical context. Co-registration with CT contributes high-resolution whole-body anatomy, enabling precise assignment of MPI hot spots to specific organs during dynamic tracking, while MRI adds high soft-tissue contrast for validating localization in the brain and other complex structures. This tri-modal MPI/CT/MRI framework strengthens the biological interpretation of cell biodistribution by combining quantitative MPI detection with spatial and anatomical fidelity. Although histological PB and HuNA staining confirm the presence of

human, iron-labeled cells, histology cannot provide whole-organ quantitative validation because it samples only thin 2D sections and may lose intravascular or weakly adherent cells during tissue processing. It requires thousands of sections, which is impossible to quantify especially when the cell distribution is inhomogeneous. Histology also detects intact cells rather than total iron mass, making it inherently incompatible with quantitative MPI signal. For these reasons, *ex vivo* MPI, which offers full-organ, background-free quantification, serves as the appropriate validation method for *in vivo* MPI cytometry and was used as such in this study.

MPI cytometry in EAE as a neuroinflammatory disease model

When we applied MPI cytometry approach in the EAE disease model, we identified a rapid redistribution of IV-delivered hMSCs from the lungs and liver to the spleen within hours (**Fig. 7**). This constitutes the first *in vivo* quantitative visualization of splenic hMSC localization in EAE using a noninvasive imaging modality, holding an important mechanistic implication. Although hMSCs rarely accumulate in the CNS in sufficient quantity to exert direct local effects, their therapeutic benefit in EAE and MS is widely believed to arise from immunomodulation within peripheral immune organs, especially the spleen (*30-32*). Our observations are consistent with prior mechanistic studies showing that, after IV administration, hMSCs can lodge within splenic immune niches and modulate systemic immunity by interacting with T-cell and macrophage populations to shift cytokine profiles and suppress pathogenic inflammation in EAE mice (*32*).

MPI cytometry provided direct evidence that a substantial fraction of hMSCs (calculated as ~12% of injected cells in our study) reaches splenic immune niches, where they may modulate T-cell and macrophage populations (*48*). Quantifying this trafficking pattern may open the door to correlating splenic stem cell load with disease severity, cytokine milieu, and therapeutic outcomes. The power of MPI cytometry lies in its ability to detect and count labeled cells in whole organs, including deep or highly vascular tissues where histology often underestimates true cell presence due to sampling limitations or post-mortem washout. Real-time MPI cytometry can inform on optimal dosing, timing, and delivery strategies for stem cell therapy, while being able to correlate variabilities in therapeutic outcome to differences in biodistribution patterns.

Clinical implications and translational outlook

Our study demonstrates a tracking platform with translational potential for integration with (stem) cell therapy. First, the tracer we employed (SPIO) is intrinsically suitable for human use. SPIO agents such as ferucarbotran, formerly used as the MRI contrast agent Resovist® and now re-introduced as Resotran® (*49*), have well-documented safety profiles in patients, and they can be used to label therapeutic cells without impairing their function (*23*). The concentration of iron per cell achieved here (tens of pg Fe/cell) is on par with that used in prior human MRI cell-tracking trials indicating that our labeling approach is scalable to clinical cell doses. Moreover, MPI itself is advancing toward clinical utilization. MPI uses low-frequency magnetic fields that are far below FDA limits and pose no known risk to tissues (*50*). Recent engineering breakthroughs have produced human-scale MPI scanners (*18-21*), and first-in-man studies are now being conducted. As a result, the combination of a non-toxic clinically approved tracer and a safe imaging modality positions MPI-based cell tracking well for rapid clinical translation.

MATERIALS AND METHODS

Study design

This study was designed to evaluate the feasibility, reproducibility and quantitative capability of *in vivo* MPI cytometry for whole-body tracking of two SPIO-labeled stem cell types (hMSCs and hNPCs) having different sizes. Cells were injected into immunodeficient Rag2$^{-/-}$ or EAE mice using either IA or IV injection. Dynamic and longitudinal MPI scans were performed to assess whole-body distribution and organ-level cell quantification, using fiducial-based calibration for standardization. MRI or CT was used for anatomical referencing, and the imaging data were verified using histological assessment.

hMSC labeling

P2 human bone marrow-derived MSCs were obtained from RoosterBio and expanded in culture up to P5 using MSC basal medium (MSCBM, Lonza) supplemented with 10% MSC growth supplement, 2% l-glutamine, 0.1% gentamicin, and 0.1% amphotericin. SPIO-labeling conditions were selected based on previous studies demonstrating no adverse effect on hMSC viability, migration, differentiation, or immunomodulatory potency when cells contain in the order of 10-30 pg iron per cell (*23, 51, 52*). To this end, hMSCs were incubated for 24 h with a pre-prepared labeling medium consisting of MSCBM medium supplemented with ferucarbotran

(25 µg Fe/ml, Meito Sangyo Co.) and poly-L-lysine (Sigma P-1524, 3 µg/ml). Following incubation, the labeling medium was removed, and the labeled hMSCs were washed three times with PBS to remove unbound particles. A total of 120,000 hMSCs were administered per IA injection, while 500,000 hMSCs were administered per IV injection.

hNPC labeling

Induced pluripotent stem cells (iPSCs) derived from a patient with amyotrophic lateral sclerosis and genetically corrected for the SOD1 mutation (39B2.5 line) were obtained from Dr. Kevin Eggan (*53*). iPSCs were differentiated into NPCs using a defined neural induction medium supplemented with dual-SMAD inhibitors (*54*). Briefly, iPSCs were plated on matrigel-coated plates and cultured to confluence in Essential 8 medium (Gibco). Neural induction was initiated using WiCell neural induction medium supplemented with dual-SMAD pathway inhibitors including LDN193189 (Stemgent) and SB431542 (Sigma). Starting on day 3, retinoic acid (Sigma) was added to promote caudalization of the neuroectoderm. On day 5, the medium was replaced with neural induction medium containing retinoic acid and continued until day 12. From day 12 to day 25, cells were maintained in neural induction medium supplemented with 1 µM purmorphamine (Sigma), 10 ng/ml BDNF (Invitrogen), 10 ng/ml GDNF (R&D Systems), 10 ng/ml CNTF (R&D Systems), 200 µM ascorbic acid (Sigma) and 10 ng/ml IGF-1 (R&D Systems) to support NPC maturation. Cells were harvested on day 25 for subsequent labeling with Synomag®-D70.

For hNPCs, the labeling procedure was performed in a standard 24-well tissue culture plate. Each well contained 100,000 hNPCs suspended in 2 ml of complete growth medium. Cells were labeled with Synomag®-D70 (40 µg Fe/ml), and poly-L-lysine (390 ng/ml). Cells were incubated for 4 h at 37°C. After incubation, cells were washed three times with 10 mM phosphate buffered saline (PBS, pH =7.2-7.4).

Extensive optimization was required to establish a robust labeling protocol for hNPCs due to their smaller size and lower endocytic volume compared to hMSCs. We evaluated multiple SPIO formulations (ferucarbotran, feraheme, Synomag®-D50, Synomag®-D70), several transfection agents (poly-L-lysine (PLL), protamine sulfate, polybrene), different culture plates, varied incubation durations (2–72 h), and physical delivery methods including electroporation and mechanoporation. None of these conditions yielded efficient intracellular

iron uptake. Synomag®-D70 combined with PLL was the only condition that consistently produced high labeling efficiency while maintaining cell viability (>90%), and this optimized protocol was therefore used for all hNPC experiments in this study.

Cell viability, Prussian blue staining and Ferrozine iron assay

To verify that SPIO labeling did not affect cell viability, we assessed hMSCs and hNPCs immediately after labeling and prior to each injection using an acridine orange/propidium iodide (AO/PI) live/dead viability kit (Logos Biosystems) and a LUNA™ dual-fluorescence automated cell counter. Labeled cells were mixed with AO/PI staining solution, loaded into a LUNA counting slide, and analyzed according to the manufacturer's protocol. Automated quantification of green (live) and red (dead) cells consistently showed >90% viability for both cell types under the labeling conditions used in this study. PB staining was performed to detect the presence of iron within labeled cells. Cells were fixed with 4% glutaraldehyde for 20 mins, washed with PBS, and incubated with Perl's reagent (potassium ferrocyanide in HCl) for 30 min at room temperature. To enhance cellular visualization, cells were counterstained with nuclear fast red (NFR) for 20 mins. Stained cells were washed with deionized water to remove excess reagent and then imaged using a Zeiss Apotome 2 microscope. The Fe content in labeled cells was determined using a Ferrozine assay as described elsewhere (*55*). A standard curve prepared with known Fe concentrations was used to calculate the Fe content in the sample.

***In vivo* injection procedures**

All animal procedures were approved by the Johns Hopkins University Animal Care and Use Committee (protocol MO24M118). Male immunodeficient Rag2$^{-/-}$ mice (6–8 weeks old, Jackson Laboratory) or female C57BL/6 mice (4-6 weeks old, Jackson Laboratory) were housed under a 12-hour light/dark cycle with ad libitum access to food and water. All injection, surgery and *in vivo* imaging procedures were performed under anesthesia using 5% induction and 1.5% maintenance isoflurane. Before injection, all labeled cell suspensions were assessed for iron content and labeling efficiency. For IA injection, the ICA was surgically catheterized as previously described (*40, 56*) and cells were delivered using a Harvard Apparatus infusion pump. IV injections were performed via a tail vein catheter and a 27G needle using the same pump system. EAE was induced in C57BL/6 mice using an MOG$_{35–55}$/CFA Emulsion kit (EK-0111,

Hooke Laboratories). Fourteen days after EAE induction, mice were catheterized in the tail vein for IV injection (n=3). Cells were suspended in 200 µl of sterile PBS and delivered IA or IV either as a single injection or in four sequential injections at 3-minute intervals for dynamic imaging studies. The infusion rate was maintained at 0.15 mL/min. Following IA injection, animals received a single subcutaneous dose of buprenorphine ER (1 mg/kg) for postoperative analgesia.

The hMSC and hNPC total doses (960,000 hNPCs vs 120,000 hMSCs) were not standardized because the two cell types differ markedly in iron-loading capacity. hMSCs efficiently internalize SPIO, whereas hNPCs load substantially less iron even under optimized Synomag®-D70/PLL conditions. Standardizing the injected cell number would therefore result in vastly different total iron doses and would place hNPCs below the MPI detection threshold. Instead, we adjusted the hNPC dose to achieve a comparable detectable iron mass.

MPI

MPI was performed using a Momentum field-free line scanner (Magnetic Insight Inc.). A custom mouse bed with two lateral racks, each featuring holes to hold fiducials, was designed in FreeCAD (v0.21.0) and fabricated using a 3D printer (Ultimaker 2 Extended+). For *in vivo* imaging, a 2D whole-body MPI scan was first acquired in standard mode, followed by a 3D scan (also in standard mode) using 21 projections. The standard mode was selected for its rapid acquisition speed, making it well suited for dynamic *in vivo* imaging (*57*). Prior to use, the imaging bed was scanned to confirm the absence of magnetic contaminants. Two fiducials containing different numbers of SPIO-labeled cells (from the same batch as those injected) suspended in 100 µL PBS were positioned within the field of view (FOV) for both MPI signal quantification and image co-registration. Regions of interest (ROIs) were manually delineated on "sharpened" MPI images using ImageJ. Windowing parameters (brightness, contrast, minimum, and maximum) were consistently adjusted across datasets acquired under the same conditions to minimize blooming artifacts, particularly in areas with high signal intensity (e.g., liver). MPI signal intensity for each hot spot was calculated by multiplying the mean signal intensity by the ROI area.

Micro-CT

Using the same *in vivo* MPI bed equipped with a custom 3D-printed adaptor for co-registration, mice were maintained under anesthesia and promptly transferred to an adjacent IVIS Spectrum/CT system (Caliper Sciences) to acquire anatomical micro-CT images. Micro-CT scans were performed with a tube voltage of 50 kVp, a current of 200 µA, and an exposure time of 300 ms. Images were acquired at a voxel resolution of 100 µm, and 3D reconstructions were generated using 3D Slicer software.

MRI

High-resolution MRI was performed *ex vivo* only. To enable co-registration of MPI and MRI data for the mouse head, a custom MPI/MRI cradle was designed using FreeCAD (v0.21.0) and fabricated with a 3D printer (Ultimaker 2 Extended+). The cradle included two alignment disks, each with a hole to hold fiducial tubes for spatial referencing. Following MPI acquisition of the excised mouse head mounted in a 3D-printed cradle, high-resolution *ex vivo* MRI was performed using a Bruker BioSpec 17.6T vertical bore scanner equipped with a Bruker BioSpin 25-mm proton transmit/receive volume coil and ParaVision 5.1 software. A 3D FLASH gradient-echo sequence was used with the following parameters: echo time=2.6 ms, repetition time=8.4 ms, flip angle=5°, FOV=20×30×18 mm^3, and matrix size=200×300×180, resulting in an isotropic spatial resolution of 100 µm. To improve the signal-to-noise ratio, 16 signal averages were acquired.

MPI/MRI and MPI/CT data co-registration

Co-registration was performed using the Volume, Look-Up Table, Transform, and Rendering tools in 3D Slicer. Two fiducial tubes containing labeled cells were included in the imaging setup and used as reference points for accurate alignment of MPI and MRI/CT datasets. When comparing MPI with MRI and CT, we did not observe major discrepancies in signal localization. However, each modality carries inherent detection biases. To minimize MPI blooming artifact from strong liver signal, sharpening and windowing parameters were kept constant across scans. As MRI hypointensities can be confounded by endogenous susceptibility sources, only MRI voids that co-localized with MPI hot spots and were confirmed by PB and anti-HuNa staining were interpreted as true positives. CT was used solely to provide anatomical reference and does not contribute to SPIO detection. In ambiguous cases, *ex vivo* MPI provided a

background-free gold standard for detection, allowing us to distinguish true signal from false positives or false negatives across modalities.

Histopathology

Following *in vivo* imaging, mice were sacrificed and transcardially perfused first with 1x PBS, followed by 4% paraformaldehyde before the brain, lungs, heart and liver were collected for *ex vivo* imaging and post-mortem analysis. Tissues were immersed in 4% PFA at 4 °C for 24 h, and then transferred to 30% sucrose for another 72 h. After embedding in optimal cutting temperature compound, the organs were sequentially cut into 20 µm sections using a cryostat (Thermo Fisher Scientific). For PB staining, tissues were fixed with 4% glutaraldehyde for 20 min and stained as described above. Anti-HuNa staining was performed to visualize hMSCs or hNPCs. Tissue sections were first blocked with 5% BSA and 0.1% Triton X-100 in Tris-buffered saline (TBS, pH=7.0) for 2 h, followed by incubation with mouse anti-HuNa (1:250, NBP2-34342, Novus-Bio). Goat anti-mouse Alexa-fluor 488 (1:500, A-11001, Invitrogen) was used as secondary antibody, prepared in 3% BSA in TBS. Sections were incubated for 2 h at room temperature and then triple washed in 1×TBS to remove unbound antibody in each step. Sections were cover-slipped with mounting medium containing DAPI. Fluorescence microscopy was performed using a Zeiss Axiovert 200 M inverted epifluorescence microscope.

Statistical analysis

Linear regression analysis was performed to plot the total MPI signal (a.u.) for each fiducial against Fe content or cell quantity. The R^2 value of each regression line was used to evaluate linearity. Data are expressed as the mean±standard deviation from at least three independent experiments (technical replicates). All statistical analysis and data visualization was performed using Microsoft Excel.

References

1. J. W. M. Bulte, H. E. Daldrup-Link, Clinical Tracking of Cell Transfer and Cell Transplantation: Trials and Tribulations. *Radiology* **289**, 604-615 (2018).
2. I. J. M. De Vries *et al.*, Magnetic resonance tracking of dendritic cells in melanoma patients for monitoring of cellular therapy. *Nature biotechnology* **23**, 1407-1413 (2005). https://doi.org/10.1038/nbt1154
3. J. Wang, J. V. Jokerst, Stem cell imaging: tools to improve cell delivery and viability. *Stem cells international* **2016**, 9240652 (2016).
4. W. J. Rogers, C. H. Meyer, C. M. Kramer, Technology insight: in vivo cell tracking by use of MRI. *Nature Clinical Practice Cardiovascular Medicine* **3**, 554-562 (2006).
5. J. W. Bulte, In vivo MRI cell tracking: clinical studies. *AJR Am J Roentgenol* **193**, 314-325 (2009).
6. L. M. Lechermann, D. Lau, B. Attili, L. Aloj, F. A. Gallagher, In vivo cell tracking using PET: Opportunities and challenges for clinical translation in oncology. *Cancers* **13**, 4042 (2021).
7. X. Zhao, Y. Ma, Z. Lei, Advanced optical imaging technology in the near infrared window for cell tracking in vivo. *Coordination Chemistry Reviews* **521**, 216178 (2024).
8. J. W. Bulte *et al.*, Quantitative "hot-spot" imaging of transplanted stem cells using superparamagnetic tracers and magnetic particle imaging. *Tomography* **1**, 91 (2015). https://doi.org/10.18383/j.tom.2015.00172
9. P. Chandrasekharan *et al.*, Magnetic particle imaging in vascular imaging, immunotherapy, cell tracking, and noninvasive diagnosis. *Molecular Imaging* **2023**, 4131117 (2023). https://doi.org/10.1155/2023/4131117
10. B. Zheng *et al.*, Magnetic particle imaging tracks the long-term fate of in vivo neural cell implants with high image contrast. *Scientific reports* **5**, 14055 (2015). https://doi.org/10.1038/srep14055
11. J. W. Bulte *et al.*, MPI Cell Tracking: What Can We Learn from MRI? *Proc SPIE Int Soc Opt Eng* **7965**, 79650z (2011). https://doi.org/10.1117/12.879844
12. G. Song *et al.*, Janus Iron Oxides @ Semiconducting Polymer Nanoparticle Tracer for Cell Tracking by Magnetic Particle Imaging. *Nano Letters* **18**, 182-189 (2018). https://doi.org/10.1021/acs.nanolett.7b03829
13. B. Gleich, J. Weizenecker, Tomographic imaging using the nonlinear response of magnetic particles. *Nature* **435**, 1214-1217 (2005).
14. J. W. M. Bulte, Superparamagnetic iron oxides as MPI tracers: A primer and review of early applications. *Adv Drug Deliv Rev* **138**, 293-301 (2019). https://doi.org/10.1016/j.addr.2018.12.007
15. M. Salimi, S. Kuddannaya, J. W. M. Bulte, Pharmacokinetic Profiling of Unlabeled Magnetic Nanoparticles Using Magnetic Particle Imaging as a Novel Cold Tracer Assay. *Nano Lett* **24**, 15557-15564 (2024). https://doi.org/10.1021/acs.nanolett.4c03553
16. M. Srinivas *et al.*, In vivo cytometry of antigen-specific t cells using 19F MRI. *Magnetic Resonance in Medicine: An Official Journal of the International Society for Magnetic Resonance in Medicine* **62**, 747-753 (2009). https://doi.org/10.1002/mrm.22063
17. O. C. Sehl, P. J. Foster, The sensitivity of magnetic particle imaging and fluorine-19 magnetic resonance imaging for cell tracking. *Scientific Reports* **11**, 22198 (2021).

18. E. Mattingly *et al.*, Design, construction and validation of a magnetic particle imaging (MPI) system for human brain imaging. *Physics in Medicine & Biology* **70**, 015019 (2025).
19. P. Vogel *et al.*, iMPI: portable human-sized magnetic particle imaging scanner for real-time endovascular interventions. *Scientific Reports* **13**, 10472 (2023). https://doi.org/10.1038/s41598-023-37351-2
20. V. Hartung *et al.*, Magnetic particle imaging angiography of the femoral artery in a human cadaveric perfusion model. *Communications Medicine* **5**, 75 (2025). https://doi.org/10.1038/s43856-025-00794-x
21. M. Graeser *et al.*, Human-sized magnetic particle imaging for brain applications. *Nat Commun* **10**, 1936 (2019). https://doi.org/10.1038/s41467-019-09704-x
22. I. Schmale *et al.*, MPI safety in the view of MRI safety standards. *IEEE Transactions on Magnetics* **51**, 1-4 (2015). https://doi.org/10.1109/TMAG.2014.2322940
23. J. W. Bulte, C. Wang, A. Shakeri-Zadeh, In vivo cellular magnetic imaging: Labeled versus unlabeled cells. *Advanced functional materials* **32**, 2207626 (2022).
24. E. Urena Horno *et al.*, Strategies towards standardizing calibration methods for magnetic particle imaging (MPI) signal quantification: solution vs. cellular environments. *Nanoscale* **17**, 24060-24071 (2025). https://doi.org/10.1039/d5nr03025k
25. M. Salimi *et al.*, MPI performance of magnetic nanoparticles depends on matrix composition and temperature: implications for in vivo MPI signal amplitude, spatial resolution, and tracer quantification. *Nanoscale Adv* **7**, 1018-1029 (2025). https://doi.org/10.1039/d4na00518j
26. B. Zheng *et al.*, Quantitative magnetic particle imaging monitors the transplantation, biodistribution, and clearance of stem cells in vivo. *Theranostics* **6**, 291 (2016). https://doi.org/10.7150/thno.13728
27. D. Karussis *et al.*, Safety and immunological effects of mesenchymal stem cell transplantation in patients with multiple sclerosis and amyotrophic lateral sclerosis. *Arch Neurol* **67**, 1187-1194 (2010). https://doi.org/10.1001/archneurol.2010.248
28. M. Neri *et al.*, Efficient in vitro labeling of human neural precursor cells with superparamagnetic iron oxide particles: relevance for in vivo cell tracking. *Stem cells* **26**, 505-516 (2008). https://doi.org/10.1634/stemcells.2007-0251
29. J. J. Gevaert, C. Fink, J. D. Dikeakos, G. A. Dekaban, P. J. Foster, Magnetic particle imaging is a sensitive in vivo imaging modality for the detection of dendritic cell migration. *Molecular Imaging and Biology* **24**, 886-897 (2022).
30. N. Song, M. Scholtemeijer, K. Shah, Mesenchymal stem cell immunomodulation: mechanisms and therapeutic potential. *Trends in pharmacological sciences* **41**, 653-664 (2020).
31. D. Zheng, T. Bhuvan, N. L. Payne, T. S. Heng, Secondary lymphoid organs in mesenchymal stromal cell therapy: more than just a filter. *Frontiers in Immunology* **13**, 892443 (2022).
32. Y. Li *et al.*, Menstrual blood-derived mesenchymal stromal cells efficiently ameliorate experimental autoimmune encephalomyelitis by inhibiting T cell activation in mice. *Stem Cell Research & Therapy* **13**, 155 (2022). https://doi.org/10.1186/s13287-022-02838-8
33. Y. Yanwu, G. Meiling, Z. Yunxia, H. Qiukui, D. Birong, Mesenchymal stem cells in experimental autoimmune encephalomyelitis model of multiple sclerosis: a systematic review and meta-analysis. *Multiple Sclerosis and Related Disorders* **44**, 102200 (2020).

34. A. Uccelli, A. Laroni, M. S. Freedman, Mesenchymal stem cells for the treatment of multiple sclerosis and other neurological diseases. *The Lancet Neurology* **10**, 649-656 (2011).
35. X. Wu *et al.*, Mesenchymal stromal cell therapies: immunomodulatory properties and clinical progress. *Stem cell research & therapy* **11**, 345 (2020). https://doi.org/10.1186/s13287-020-01855-9
36. M. Sanchez-Diaz *et al.*, Biodistribution of mesenchymal stromal cells after administration in animal models and humans: a systematic review. *Journal of clinical medicine* **10**, 2925 (2021). https://doi.org/10.3390/jcm10132925
37. B. B. Chin *et al.*, 111In oxine labelled mesenchymal stem cell SPECT after intravenous administration in myocardial infarction. *Nucl Med Commun* **24**, 1149-1154 (2003). https://doi.org/10.1097/00006231-200311000-00005
38. D. L. Kraitchman *et al.*, Dynamic imaging of allogeneic mesenchymal stem cells trafficking to myocardial infarction. *Circulation* **112**, 1451-1461 (2005). https://doi.org/10.1161/CIRCULATIONAHA.105.537480
39. B. Argibay *et al.*, Intraarterial route increases the risk of cerebral lesions after mesenchymal cell administration in animal model of ischemia. *Scientific reports* **7**, 40758 (2017). https://doi.org/10.1038/srep40758
40. M. Janowski *et al.*, Cell size and velocity of injection are major determinants of the safety of intracarotid stem cell transplantation. *J Cereb Blood Flow Metab* **33**, 921-927 (2013). https://doi.org/10.1038/jcbfm.2013.32
41. C. Bos *et al.*, In vivo MR imaging of intravascularly injected magnetically labeled mesenchymal stem cells in rat kidney and liver. *Radiology* **233**, 781-789 (2004). https://doi.org/10.1148/radiol.2333031714
42. V. Sood *et al.*, Biodistribution of 18F-FDG-labeled autologous bone marrow–derived stem cells in patients with type 2 diabetes mellitus: exploring targeted and intravenous routes of delivery. *Clinical Nuclear Medicine* **40**, 697-700 (2015). https://doi.org/10.1097/RLU.0000000000000850
43. J. Ge *et al.*, The size of mesenchymal stem cells is a significant cause of vascular obstructions and stroke. *Stem cell reviews and reports* **10**, 295-303 (2014). https://doi.org/10.1007/s12015-013-9492-x
44. A. Remmo *et al.*, Counting cells in motion by quantitative real-time magnetic particle imaging. *Scientific Reports* **14**, 4253 (2024). https://doi.org/10.1038/s41598-024-54784-5
45. R. M. Ferguson *et al.*, Magnetic particle imaging with tailored iron oxide nanoparticle tracers. *IEEE transactions on medical imaging* **34**, 1077-1084 (2014). https://doi.org/10.1109/TMI.2014.2375065
46. L. M. Bauer, S. F. Situ, M. A. Griswold, A. C. S. Samia, Magnetic particle imaging tracers: state-of-the-art and future directions. *The journal of physical chemistry letters* **6**, 2509-2517 (2015).
47. G. C. de Albuquerque Souza, R. M. G. Gontijo, J. B. da Silva, M. Mamede, A. V. Ferreira, Spatial resolution of a preclinical PET tomograph. *Brazilian Journal of Radiation Sciences* **9**, (2021).
48. Z. Wang *et al.*, The spleen may be an important target of stem cell therapy for stroke. *Journal of Neuroinflammation* **16**, 20 (2019). https://doi.org/10.1186/s12974-019-1400-0

49. F. Mohn *et al.*, Characterization of the clinically approved MRI tracer resotran for magnetic particle imaging in a comparison study. *Phys Med Biol* **69**, (2024). https://doi.org/10.1088/1361-6560/ad5828
50. M. Irfan, N. Dogan, Comprehensive evaluation of magnetic particle imaging (MPI) scanners for biomedical applications. *Ieee Access* **10**, 86718-86732 (2022).
51. G. Schmidtke-Schrezenmeier *et al.*, Labeling of mesenchymal stromal cells with iron oxide–poly (L-lactide) nanoparticles for magnetic resonance imaging: uptake, persistence, effects on cellular function and magnetic resonance imaging properties. *Cytotherapy* **13**, 962-975 (2011). https://doi.org/10.3109/14653249.2011.571246
52. B. Addicott *et al.*, Mesenchymal stem cell labeling and in vitro MR characterization at 1.5 T of new SPIO contrast agent: Molday ION Rhodamine-B™. *Contrast Media & Molecular Imaging* **6**, 7-18 (2011). https://doi.org/10.1002/cmmi.396
53. E. Kiskinis *et al.*, Pathways disrupted in human ALS motor neurons identified through genetic correction of mutant SOD1. *Cell stem cell* **14**, 781-795 (2014). https://doi.org/10.1016/j.stem.2014.03.004
54. S. M. Chambers *et al.*, Highly efficient neural conversion of human ES and iPS cells by dual inhibition of SMAD signaling. *Nature biotechnology* **27**, 275-280 (2009). https://doi.org/10.1038/nbt.1529
55. J. W. Bulte, G. F. Miller, J. Vymazal, R. A. Brooks, J. A. Frank, Hepatic hemosiderosis in non-human primates: quantification of liver iron using different field strengths. *Magnetic resonance in medicine* **37**, 530-536 (1997).
56. P. Walczak *et al.*, Dual-modality monitoring of targeted intraarterial delivery of mesenchymal stem cells after transient ischemia. *Stroke* **39**, 1569-1574 (2008). https://doi.org/10.1161/STROKEAHA.107.502047
57. A. Shakeri-Zadeh, S. Kuddannaya, A. Bibic, J. W. Bulte, Spillover can limit accurate signal quantification in MPI. *npj Imaging* **3**, 1-9 (2025).

Acknowledgments

We thank Dr. Adnan Bibic for his valuable assistance with the MRI experiments and Dr. Yuguo Li for his experimental assistance with the animal studies.

Funding: This work was supported by grants from the National Institutes of Health (UH2/UH3 EB028904 (JWMB), S10 OD026740 (JWMB) and the Maryland Stem Cell Research Fund MSCRFD-5416 (JWMB) and MSCRFL-6270 (ASZ). As this manuscript is the result of funding in whole or in part by the National Institutes of Health (NIH), it is subject to the NIH Public Access Policy. Through acceptance of this federal funding, NIH has been given a right to make this manuscript publicly available in PubMed Central upon the Official Date of Publication, as defined by NIH.

Author contributions:

Conceptualization: JWMB, ASZ, SK, PW

Methodology: JWMB, ASZ, SK, PW

Investigation: ASZ, SK, CC, KS, AI, AMT, PW, JWMB

Visualization: ASZ, SK, CC, KS, AI, PW, JWMB

Funding acquisition: JWMB, ASZ

Project administration: JWMB

Supervision: ASZ, JWMB

Writing – original draft: ASZ, JWMB

Writing – review & editing: ASZ, SK, CC, KS, AI, AMT, PW, JWMB

Competing interests: J.W.M.B. is a shareholder of SuperBranche. This arrangement has been reviewed and approved by Johns Hopkins University in accordance with its conflict-of-interest policies. Piotr Walczak is a founder and holds equity in IntraArt, LLC and Ti-com, LLC. Other co-authors have no competing interest to disclose.

Data and materials availability: All data are available in the main text.